Measured Dependence of Nuclear Burn Region Size on Implosion Parameters in Inertial Confinement Fusion Experiments

Introduction

Images of the nuclear burn regions in inertial confinement fusion (ICF) capsules are important for fully assessing the combined results of all the complicated processes that affect capsule implosion dynamics; these processes, including drive, preheat, instabilities, and mix, must be understood and controlled to achieve ignition and energy generation.[1–3] In the direct-drive approach to ICF, a spherical capsule containing fuel is compressed and heated by direct illumination of laser beams focused on the capsule surface in a nominally uniform fashion.[2] Hydrodynamic instabilities affect the performance of these implosions,[2–10] ultimately determining the size, symmetry, and yield of the nuclear burn region. This article, the third in a series about proton emission imaging,[11–13] presents the first comprehensive studies of D^3He burn region sizes in nominally symmetric direct-drive implosions with diverse capsule and drive conditions. Radial burn profiles and total yields are obtained from measurements of energetic 14.7-MeV protons from the fusion of deuterium (D) and 3-helium (^{3}He) using methods described in Refs. 11 and 12 and in the appendix (see p. 10) of this article. Complementary data from x-ray images,[14–17] proton spectrometers,[18–23] and clean 1-D simulations[24,25] are used in interpreting the burn region sizes and their implications. Asymmetric burn distributions and their relationships to capsule and drive parameters are described in Refs. 11 and 13, and tests of the fidelity of the reconstructed images are discussed in Refs. 11 and 12. Burn images have previously been made of deuterium–tritium-filled capsules using 14.1-MeV neutrons,[8,26–29] 3-MeV protons,[30–32] or 3.5-MeV alpha particles,[32] but for a more limited range of implosion types (see also other papers cited in Ref. 11).

Experimental Conditions (p. 1) describes the drive and capsule parameters studied along with general information about the proton emission imaging cameras and the other diagnostics used. **Data Analysis** (p. 2) provides an overview of the analysis of proton imaging data with examples from two implosions that have dramatically different burn regions. Similarities and differences between nuclear burn images and x-ray images are discussed and important connections between burn profiles, areal density (ρR), and clean 1-D simulations are made. **The Dependence of R_{burn} on Laser and Capsule Parameters** (p. 5) summarizes the results obtained when capsule and drive conditions were systematically varied. The dependence of the burn radius on shell thickness, gas pressure, laser energy, and shell type is investigated for a large set of implosions and evidence of the presence of mix is discussed. **Summary and Discussion** (p. 9) details the results and future work, and the appendix (p. 10) provides detailed information about methods of calculating radial burn profiles from penumbral images (including neutron images).

Experimental Conditions

To explore the range of burn region sizes associated with different kinds of symmetrically driven implosions, and to reveal effects of complicated physics such as preheat, mix, drive efficiency, and core distortions, a wide variety of implosions were examined on the OMEGA Laser System.[33] OMEGA is a 60-beam, frequency-tripled, UV (0.35-μm) laser capable of delivering up to 30 kJ of laser energy in a variety of pulse shapes. The individual laser beams were smoothed with distributed phase plates (DPP's),[34] 2-D smoothing by spectral dispersion with a bandwidth of 1.0 THz,[35,36] and polarization smoothing using birefringent wedges.[37] Two types of DPP's (SG3 and SG4) were used in the experiments described here, producing different beam-intensity profiles.[38] Only 1-ns square laser pulses were used to directly illuminate the capsule. The beam-to-beam energy imbalance was typically less than 4% rms.

The capsules used either 1.8- to 2.3-μm-thick glass (SiO_2) shells filled with 18-atm D^3He gas or 17- to 24-μm-thick plastic (CH) shells filled with 3.6- or 18-atm D^3He gas. The glass-shell implosions used SG3 DPP's while the thick plastic-shell implosions used SG4 DPP's, except where noted. Initial capsule radii were nominally 470 μm for the SG3 DPP's and 430 μm for SG4 DPP's.

Proton core imaging system (PCIS) cameras[11–13] imaged the time-integrated D^3He proton emission distribution from

up to three nearly orthogonal directions simultaneously. These are penumbral imaging cameras, each consisting of a round imaging aperture that is significantly larger than the size of the D^3He burn region and a detector pack comprised of several ranging filters and CR-39 charged-particle detectors.[12,19] The distances from the implosion to the imaging aperture and from the imaging aperture to the detector pack (L_1 and L_2, respectively) determine the geometric magnification $M \equiv L_2/L_1$. Aperture diameters of 600 μm and 2000 μm were used; L_1 was typically 3 cm and M varied from 8 to 20. The energetic protons that pass through the aperture are detected with 100% efficiency in the CR-39 as long as the detector has filtering that slows incoming protons down to the CR-39 sensitivity range of about 0.5 to 8 MeV.

X-ray framing cameras were used to obtain 4- to 5-keV x-ray emission images[14–16] at 58-ps time intervals using 12× magnification and 40-ps integration times. At the time of peak proton production, the x-ray images represent primarily continuum emission from the heated inner portion of the shell material and can be used to estimate the radius of the fuel–shell interface, as described in Ref. 14.

Up to five proton spectrometers[19] were used simultaneously to obtain time-integrated measurements of the D^3He proton spectrum. These spectra are used to determine the total areal density $\langle \rho R \rangle$[19,23,39] using the downshift from the 14.7-MeV birth energy.[18–22,39] In these experiments the measured total ρR comprises both the shell ρR and the fuel ρR, but is usually dominated by the shell.[19,23,39] For given capsule shell and laser conditions, ρR provides a measure of shell convergence since, all else being equal, ρR scales as the inverse of the square of the shell radius at the time of burn. The PCIS and spectrometers typically give the same D^3He yield to within the observed proton-yield asymmetry of 15% to 20% rms.[19]

Data Analysis

1. Finding the Nuclear Burn Radius R_{burn}

The proton emission imaging cameras produce time-integrated penumbral images that are processed to produce either a 2-D image of the burn region surface brightness in D^3He reactions per unit area, $B(r,\phi)$, or a 1-D radial profile of the local number of D^3He reactions per unit volume, $S(r)$, which corresponds to an average over angles. The 2-D analysis technique is extremely useful for studying low-mode deviations from spherical symmetry, and simultaneous views of the burn region from three orthogonal directions can provide measurements of a 3-D structure; this approach has been used to study the important effects of asymmetric laser drive and asymmetric shell structure on implosion symmetry.[13] A disadvantage of 2-D image reconstruction is that it always requires significant smoothing for control of statistical noise, as described in detail in Ref. 11. For the types of implosions studied at OMEGA, D^3He burn region sizes and yields typically require smoothing that limits the 2-D spatial resolution to the range of 15 to 30 μm. If it is desired to make an accurate measurement of characteristic burn region size for nearly symmetric implosions, it is advantageous to use the 1-D approach; it avoids smoothing errors and typically results in statistical measurement uncertainties of a few microns. Since the object of this article is to study burn region size, we will use 1-D analysis here and discuss 2-D results elsewhere.[13]

The 1-D reconstruction approach utilizes the relationship between $S(r)$ and the radial derivative dN/dR of the penumbral image values N (proton tracks per unit area on the detector); dN/dR is equivalent to a set of line integrals through the surface brightness of the D^3He burn region, as discussed in detail in Ref. 11 and in the appendix (p. 10). Of the two 1-D methods described in the appendix, we will use the method of fitting dN/dR with a family of functions that correspond either analytically or numerically to a family of local burn profile shapes.[11] The radial profile $S(r)$ of the proton source in reactions per unit volume is represented by a member of the family of super-Gaussians and sub-Gaussians

$$S(r) = S_0 e^{-(r/r_0)^{2/p}}, \tag{1}$$

where p is a "peakedness" shape parameter and r_0 is a measure of burn radius. The median radius R_{burn} containing half of the total local emission is actually used rather than r_0 to characterize the burn region size because it can be determined much more accurately and is nearly independent of the emission profile shape (see the appendix on p. 10). The burn profile parameters and geometric parameters are then varied to generate the best fit between the measured and predicted dN/dR.

Figure 105.1 shows sample data from two very different implosions involving capsules whose shells are 2-μm-thick glass [Fig. 105.1(a)] and 20-μm-thick plastic [Fig. 105.1(e)]. The plotted data show dN/dR from the azimuthally averaged penumbral images with error bars representing statistical uncertainties. For each data set, a best fit (solid line) was found and used to determine the absolute radial profile of the burn [Figs. 105.1(c) and 105.1(g)] and its characteristic radius R_{burn} as well as the absolute radial profile of surface brightness $B(r)$ [Figs. 105.1(d) and 105.1(h)]. The values of R_{burn} were 29±2.5 μm for the plastic-shell implosion and 54±2 μm for

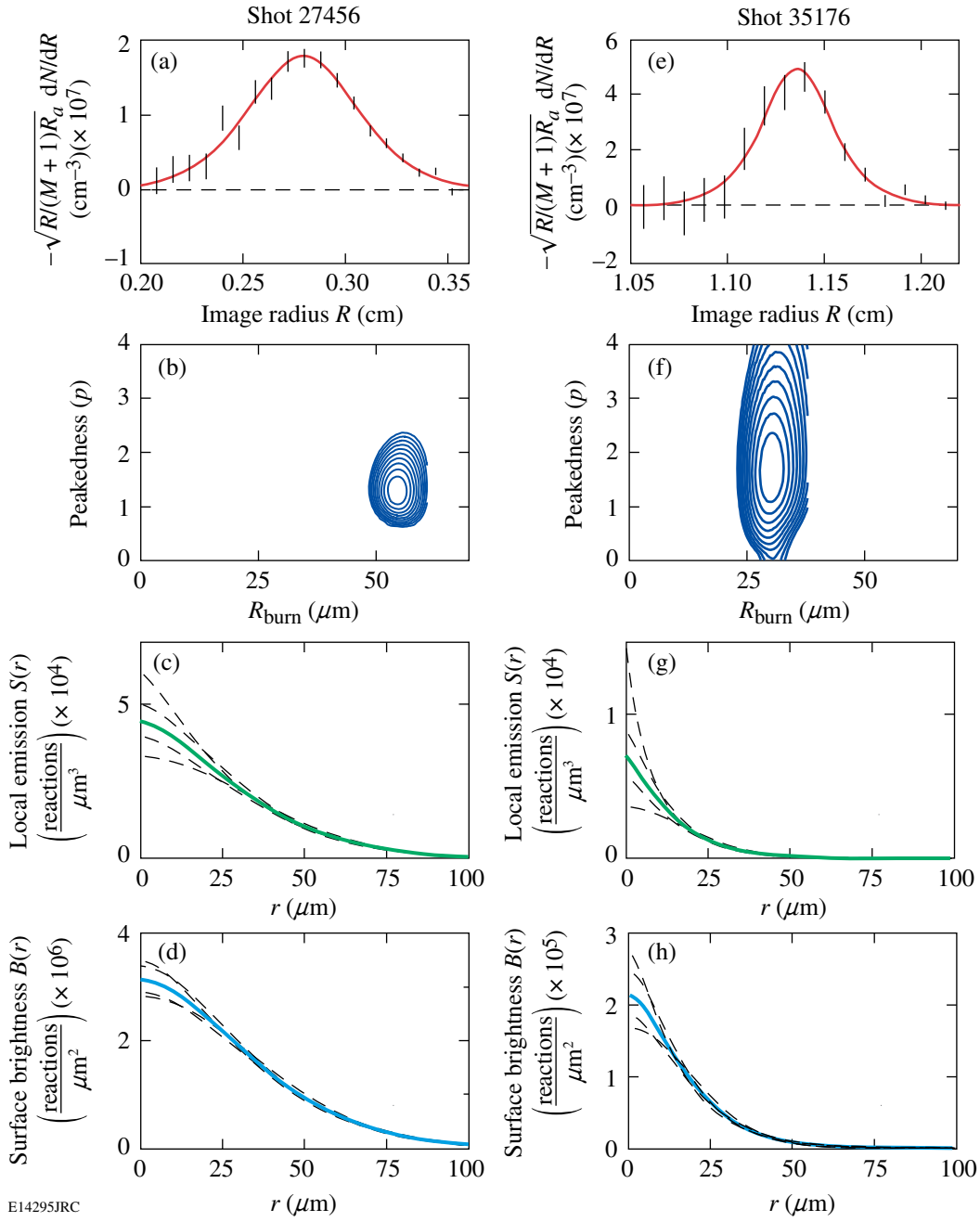

Figure 105.1

Data illustrating the burn region analysis of two very different implosions on OMEGA. The left-hand column corresponds to shot 27456 (2-μm-thick, glass-shell capsule), while the right-hand column corresponds to shot 35176 (20-μm-thick, plastic-shell capsule); each capsule was filled with 18-atm D^3He and irradiated with a 23-kJ, 1-ns laser pulse. The vertical lines in (a) and (e) represent statistical error bars for measured values of dN/dR; the locations of all individual proton tracks on the penumbral image detector are measured to a fraction of a micron, but $N(R)$ needs to be binned with a finite interval in R to achieve acceptable statistics. Note that the significance of the square root appearing as a coefficient dN/dR in the vertical axis labels is discussed in the appendix (p. 10) in connection with Eq. (14); this slowly varying coefficient is very close to 1.0 for the data shown here. The thick lines in (a) and (e) are best fits to the data using the approach described in **Data Analysis** (p. 2) and in the appendix (p. 10). Contour plots showing the total χ^2 as a function of R_{burn} and peakedness p are shown in (b) and (f); the contour levels correspond to $\chi^2_{minimum}+1, \chi^2_{minimum}+2, \ldots$. In (c) and (g) the inferred radial distributions $S(r)$ of D^3He reactions in the burn regions are shown; each thick line corresponds to a best fit while the thin dashed lines show alternate fits resulting in the total χ^2 being larger than the minimum value by 1 (indicating an approximate error envelope for the best-fit profile). The corresponding surface brightness distributions $B(r)$ are shown in (d) and (h). The parameters describing the profiles $S(r)$ are R_{burn} = 54±2 μm and p = 1.35±0.25 (shot 27456) and R_{burn} = 29±2.5 μm and p = 1.7±0.6 (shot 35176).

the glass-shell implosion (where the errors quoted here and throughout reflect statistical uncertainties). As discussed in the appendix (p. 10), the shapes of the radial profiles have their largest uncertainties at $r = 0$ and the values of R_{burn} are determined much more accurately than the shape parameter.

While multiple imaging cameras are generally used to study implosion asymmetry, a single camera provides enough information to calculate a 1-D emission profile of a nominally symmetric capsule implosion. When data from more than one camera were available for an individual implosion studied in this article, the images were analyzed separately and the values of R_{burn} were averaged.

2. Comparing Nuclear Burn Data with X-Ray Data

Since x-ray imaging has been a standard diagnostic technique for decades, it is important to compare x-ray and fusion-burn profiles even though they have very different sensitivities to plasma processes and parameters. They provide valuable and complementary spatial information. The fusion burn profile $S(r)$ represents the time-integrated spatial distribution of the nuclear reaction rate

$$RR = N_D N_{3_{\text{He}}} \langle \sigma v \rangle_{\text{D}^3\text{He}}, \qquad (2)$$

where N_D and $H_{3_{\text{He}}}$ are the D and ^{3}He ion number densities and $\langle \sigma v \rangle$ is the reaction rate for the D^{3}He reaction. In contrast, x-ray images primarily record emissions from heated CH near the fuel–shell interface.[14] In addition, the burn data are time integrated while the x-ray images are gated with a 40-ps window[16] (and show slightly decreasing size during the ~150-ps burn interval). Figure 105.2 provides a comparison between burn data and an x-ray image taken approximately at peak burn time for shot 35176 (analyzed in Fig. 105.1). Although the image of x-ray surface brightness itself [Fig. 105.2(b)] isn't quite symmetric, its azimuthally averaged radial profile allows us to estimate that the fuel–shell interface was located approximately at the radius $R_{\text{xray}} = 32 \pm 5$ μm where the brightness peaks before decreasing with increasing radius.[14] The value of R_{burn} was 29±2.5 μm; considering the different nature of the two kinds of data and the ambiguities as to exactly how they should be compared, the two measurements appear approximately consistent with each other. We will see in **The Dependence of R_{burn} on Laser and Capsule Parameters** (p. 5) that the x-ray and nuclear burn profile data respond in a similar fashion to changes in the experimental conditions for a variety of implosions.

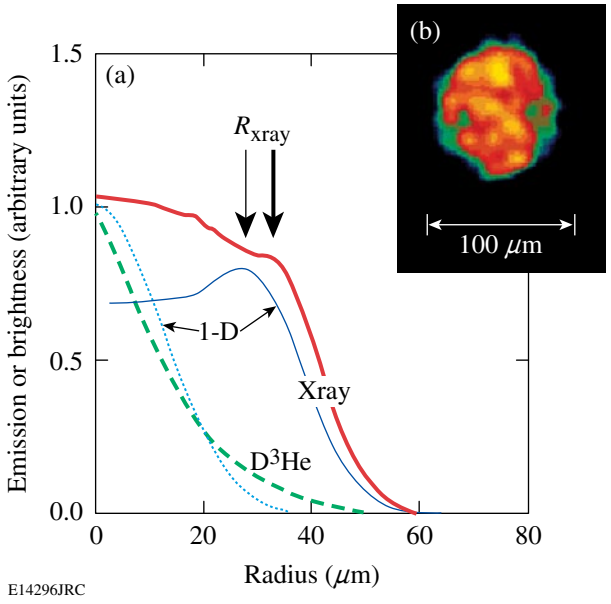

Figure 105.2
Comparison of the measured local D^{3}He emission profile, the measured x-ray surface brightness profile, and 1-D simulations for shot 35176. A 4- to 5-keV x-ray image taken at the peak nuclear burn time (a 40-ps exposure) is shown in (b), and its radial profile is shown in (a) along with a 1-D simulation (solid lines). The D^{3}He burn profile [from Fig. 105.1(g)] is also shown in (a) along with a 1-D simulation (broken lines). In all cases, the measured profiles are thick lines and the 1-D profiles are thin lines. The D^{3}He profiles are arbitrarily normalized to have the same value at $r = 0$.

3. Comparing Nuclear Burn Data and X-Ray Data with 1-D Simulations

The burn data and x-ray data can also be compared to clean 1-D simulations,[24,25] keeping in mind the fact that these simulations don't properly model such important physical processes as fuel–shell mix, preheat, or any type of implosion asymmetry and that they nearly always overestimate the nuclear burn yield.[4] In Fig. 105.2 the measured local burn profile and the measured x-ray surface brightness profile for the plastic-shell implosion 35176 are compared to simulations. The predicted value of R_{xray} is slightly smaller than the measured value (by about 15%). The predicted profile of the D^{3}He burn is quite similar in shape to the measured profile in the core [although the measured shape uncertainty is large there, as shown in Fig. 105.1(g)], but the measured emission values are considerably higher than predicted at larger radii where they contribute heavily to the yield-weighted R_{burn}: the predicted R_{burn} is about 25% smaller than the measured value. On the other hand, there are other indications that the 1-D predictions aren't exactly right: the predicted yield is about 150% higher than the measured value, while the predicted shell

areal density is 26% larger than the measured value (indicating that the shell did not converge radially as much as predicted). It will be seen in **The Dependence of R_{burn} on Laser and Capsule Parameters** (p. 5) that measured values of R_{burn} are uniformly larger than simulated values for the CH-shell implosions studied here but that the measured and predicted values agree fairly well for a wide range of glass-shell implosions (which have different implosion dynamics[40]). Possible explanations of this measurement/simulation discrepancy in terms of either systematic measurement errors (of which we have no evidence[41]) or effects not included in 1-D simulations (mix, preheat, and hydrodynamic instabilities) are considered in **Summary and Discussion** (p. 9).

The Dependence of R_{burn} on Laser and Capsule Parameters

Correlations between R_{burn} and the capsule and drive conditions allow an elucidation of some basic implosion dynamics. Systematic studies that examine the dependence of R_{burn} on laser drive energy, capsule shell material and thicknesses, capsule fill pressure, and DPP type are presented here. These external parameters are often strongly correlated with one or more fundamental quantities or processes such as ion temperature, capsule convergence, fuel density, and fuel–shell mix. For that reason, attempts were made to change only one external parameter at a time in experiments whenever possible.

1. Laser Energy

Figure 105.3(a) shows the effect of increasing laser energy for 1-ns square pulses when irradiating thin glass-shell capsules. As the energy was increased from 6 kJ to 23 kJ, R_{burn} increased from about 35 μm to 80 μm. For capsules with 19- to 20-μm CH shells and 18-atm D^3He fills, R_{burn} was about 30 μm; data are not yet available for illustrating variations with laser energy. The change in yield-weighted ion temperature $\langle T_{ion} \rangle$ [42] probably dominates the change in R_{burn} for the glass-shell capsules, as illustrated in Fig. 105.3(b) where the data of Fig. 105.3(a) are replotted as a function of $\langle T_{ion} \rangle$. Increases in $\langle T_{ion} \rangle$ should result in a larger R_{burn} since the D^3He reactivity is extremely sensitive to the ion temperature. Figure 105.3(c) replots the data of Fig. 105.3(a) with the corresponding R_{burn} values from 1-D simulations. For the glass shells, 1-D simulations agree fairly well with R_{burn} measurements and show the same variation with laser energy; for the plastic shells, the 1-D values are uniformly lower than the measured R_{burn} values.

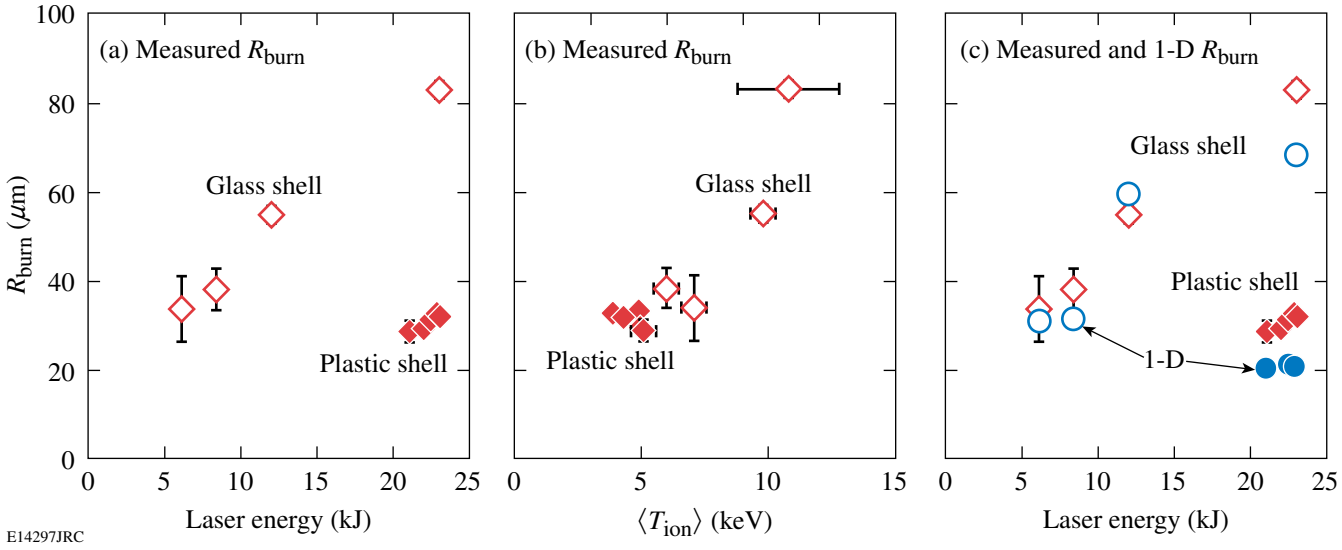

Figure 105.3
(a) Data showing the relationship of burn region size to laser energy for implosions of capsules with an 18-atm D^3He fill and either 20-μm plastic or 2-μm glass shells. For the thin-glass-shell, exploding-pusher implosions (open diamonds), increasing the laser energy results in a dramatically larger D^3He burn region radius. For the thick-CH-shell, compressive implosions, $R_{burn} \approx 30$ μm for 23-kJ laser energy (solid diamonds), but data are not currently available for lower laser energies. The ion temperature was strongly correlated with R_{burn}, as shown in (b) where R_{burn} has been plotted versus the burn-averaged ion temperature $\langle T_{ion} \rangle$ obtained with neutron time-of-flight systems. (c) Comparison of R_{burn} measurements with values from 1-D simulations (circles).

2. Capsule Fill Pressure

The effects of fill pressure changes on R_{burn} for CH-shell implosions were studied systematically. Figure 105.4(a) shows R_{burn} plotted as a function of measured $\langle \rho R \rangle$ for fill pressures of 3.6 atm and 18 atm. R_{burn} is consistently larger for the higher fill pressure. Figure 105.4(b) shows the averages of the measured values[43] for all implosions of each fill pressure in Fig. 105.4(a); the plotted values are

$$\langle R_{burn}\,(18\text{ atm})\rangle = 30.6 \pm 0.3\ \mu\text{m} \tag{3}$$

and

$$\langle R_{burn}\,(3.6\text{ atm})\rangle = 24.8 \pm 0.8\ \mu\text{m}, \tag{4}$$

where the quoted errors reflect only the statistical uncertainties and do not include any other possible systematic errors. Figure 105.4(b) also shows corresponding values of R_{xray} for which we have data. The same trend is seen in both R_{burn} and R_{xray}. Figure 105.4(c) compares values of R_{burn} and $\langle \rho R \rangle$ from 1-D simulations (solid circles for 18 atm and open circles for 3.6 atm) to the data. While the measured R_{burn} values are all larger than predicted (as for all other plastic-shell implosions studied here), there are other important differences between simulations and measurements. The 1-D simulations predict that a reduction in fill pressure from 18 atm to 3.6 atm should result in a large increase in ρR (by ~93%) due to increased radial convergence of the shell material accompanied by a substantial decrease in R_{burn} (by ~40%) largely due to a corresponding decrease in the core size. In contrast, the data indicate a much smaller increase in ρR (by ~13%), implying little change in radial convergence of the bulk of the shell material and a moderate decrease in R_{burn} (by ~20%).

These results agree quite well with data and interpretations published by C. K. Li *et al.*[4] for implosions of plastic-shell capsules with DT fills of various pressures. For laser conditions and shell thicknesses similar to those examined here, it was concluded that the experimental radial convergence increased only slightly when the pressure was reduced from ~18 to 3 atm, in distinct contrast to 1-D calculations, exactly as seen here; it was suggested that the failure to achieve higher radial shell convergence with a low fill pressure was probably due to the fuel–shell mix, which converts some of the kinetic energy of radial shell movement to lateral motion. This is also consistent with the present data, which show a significant reduction in measured R_{burn} when the pressure was decreased in spite of little change in the compressed shell radius; if the radius of most of the shell is held fixed, cooling and dilution of the outer fuel region due to the mixing in of a small amount of cooler shell

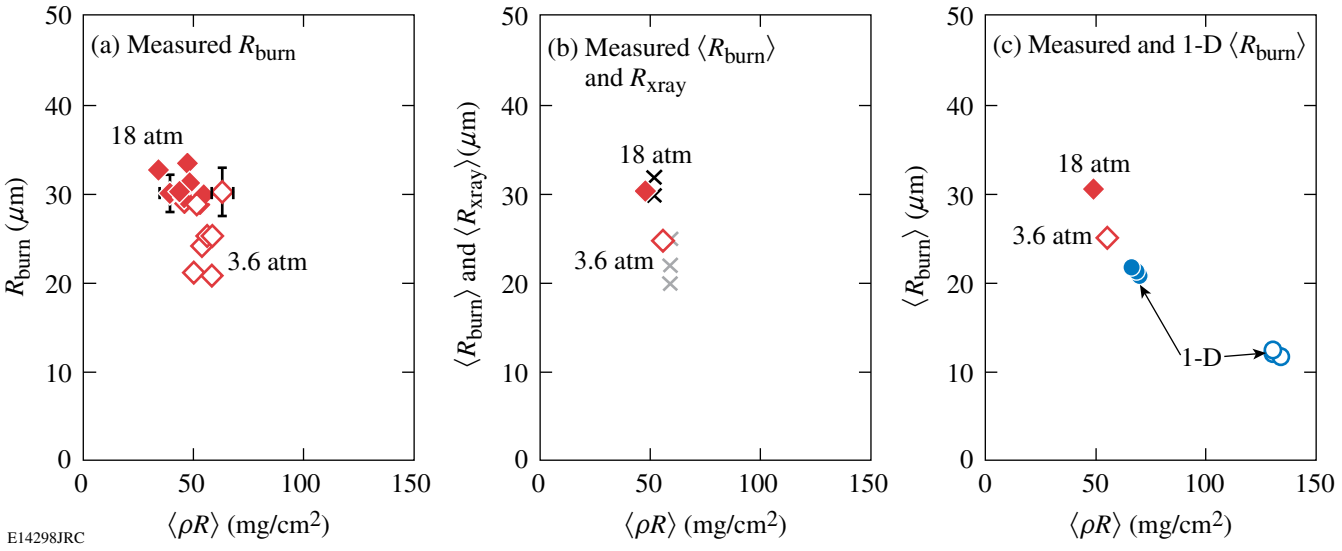

Figure 105.4

(a) A significant difference in the D^3He burn size is shown for 18-atm (solid diamonds) and 3.6-atm (open diamonds) fill pressures in implosions of D^3He-filled capsules with 19- to 20-μm plastic shells. R_{burn} is plotted as a function of the areal density $\langle \rho R \rangle$ measured from proton energy downshifts. (b) The averages of data in (a) are displayed with fuel–shell interface estimates (R_{xray}) for 18-atm (black ×'s) and 3.6-atm (gray ×'s) implosions, demonstrating agreement in the trends of both R_{burn} and R_{xray}. (c) When the average data are displayed with the 1-D calculated R_{burn} (circles), the same trend is present but the simulations predict lower R_{burn} values overall and a much larger increase in ρR with decreased fill pressure.

material would reduce the number of D^3He reactions there and reduce R_{burn}. The 1-D simulations predict a much larger decrease in R_{burn} at a lower fill pressure without invoking mix, but this is because they predict a much larger increase in radial convergence than is measured.

Finally, it seems plausible that the increased scatter of R_{burn} at lower pressures may reflect decreased stability for those implosions. As shown in Fig. 105.4(a), the standard deviation in the 3.6-atm data is larger than that for the 18-atm data (by the ratio of 3.6 μm to 1.4 μm).

3. Distributed Phase Plates

An important goal of the OMEGA program is to improve the single and overlapping beam uniformity of the laser. As a step in that direction, the older SG3 DPP's were recently replaced with SG4 DPP's that result in a flatter on-target beam intensity [$\propto e^{-(r/353\ \mu\text{m})^{4.1}}$, where r is radius from beam center, rather than $e^{-(r/308\ \mu\text{m})^{2.2}}$ with the SG3 DPP].[38] To adjust for a reduction in the new spot size, the capsule radii were also reduced from ~470 to 430 μm. Figure 105.5 shows the effect of these changes on R_{burn} for several shots, plotted as a function of ρR. R_{burn} is larger for the SG3 data than for the SG4 data. The average measurement values[43] of all implosions shown in Fig. 105.5(a) are

$$\langle R_{burn}\,(\text{SG3})\rangle = 37.1\pm0.8\ \mu\text{m} \tag{5}$$

and

$$\langle R_{burn}\,(\text{SG4})\rangle = 30.5\pm0.3\ \mu\text{m} \tag{6}$$

and are plotted in Fig. 105.5(b). The fact that convergence, determined from ρR,[4] is about the same for the SG3 and SG4 implosions, suggests that the reduction in R_{burn} for the SG4 DPP is largely a consequence of the smaller initial capsule radius (this is consistent with other measurements,[44] indicating that changing from SG3 DPP's to SG4 DPP's brought no significant improvement in overall implosion performance for capsules with 20-μm CH shells and 18-atm fills). The values of R_{xray} show the same kind of variation with DPP type as the values of R_{burn}, as shown in Fig. 105.5(b).[45] The 1-D R_{burn} simulations [Fig. 105.5(c), open circles for SG3 and solid circles for SG4] don't show as large a change with DPP type as the measured R_{burn} or R_{xray}. An interesting question to address would be whether the SG4 DPP reduces the scatter in 3.6-atm

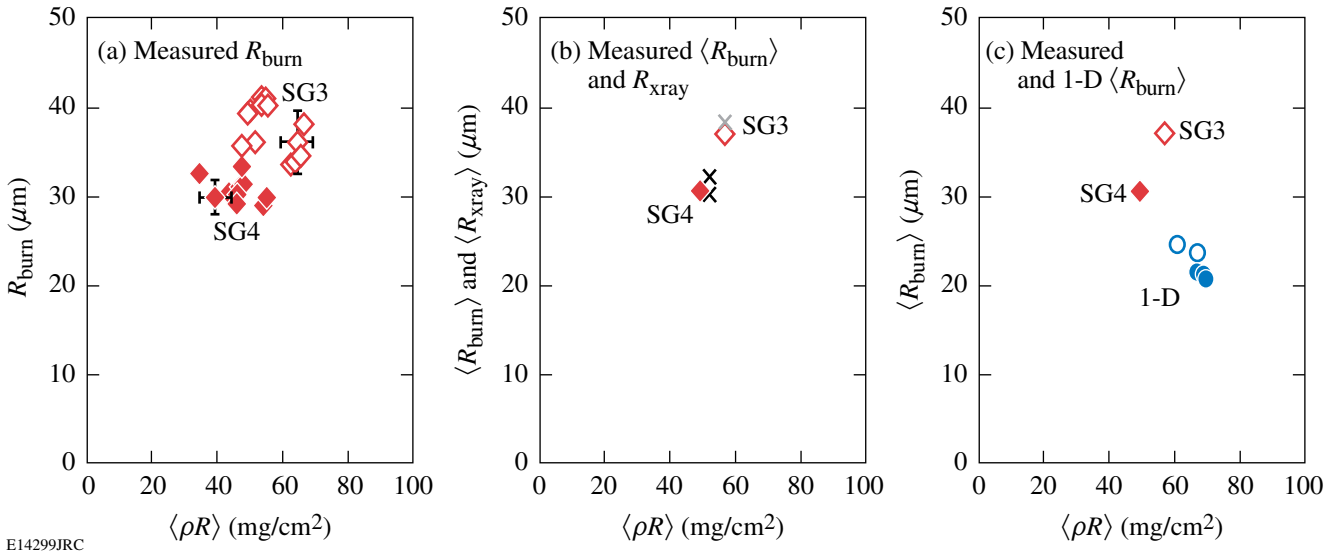

Figure 105.5
(a) Consistently smaller burn radii are produced with SG4 phase plates and targets (solid diamonds) than with SG3 DPP's (open diamonds). R_{burn} is plotted as a function of the measured areal density ρR for implosions of capsules with 19- to 20-μm-thick plastic shells and 18-atm D^3He fill. (b) The averages of burn radii data in (a) are displayed with fuel–shell interface estimates (R_{xray}) from SG3 (gray ×) and SG4 (black ×) implosions,[44] demonstrating agreement in the trends of R_{burn} and R_{xray}. (c) When the average R_{burn} data are displayed with the 1-D values (circles) the same trend is present but the simulations predict lower R_{burn} values and a smaller change in R_{burn} with the change in phase plates. The reduction in R_{burn} with the change from SG3 to SG4 DPP's seems largely dominated by the reduction in initial capsule radius from ~470 to 430 μm.

capsule performance that was discussed in connection with Fig. 105.4, but comparative data are currently unavailable.

4. Capsule Shell Thickness

The shell thickness is known to have an effect upon mix and convergence.[4–9,10] Figure 105.6(a) shows the effect on R_{burn} (diamonds). The trend of these data is more fully revealed by averaging the data over capsules with similar shell thicknesses [Fig. 105.6(b)]. As illustrated, R_{burn} increases slowly as the shell thickness increases from 17 to 24 μm with the values

$$\langle R_{burn}\,(17\ \mu\text{m})\rangle = 29.1\pm0.4\ \mu\text{m}, \tag{7}$$

$$\langle R_{burn}\,(20\ \mu\text{m})\rangle = 30.5\pm0.5\ \mu\text{m, and} \tag{8}$$

$$\langle R_{burn}\,(24\ \mu\text{m})\rangle = 32.8\pm1.1\ \mu\text{m}. \tag{9}$$

The convergence for the thicker-shell capsules was slightly smaller, as reflected in the fact that the ρR's of those capsules are about the same [Fig. 105.6(c)];[4] the larger burn radii for the thicker 24-μm capsules reflect the smaller convergence. R_{xray}, also plotted in Fig. 105.6(b), shows a similar trend. R_{burn} for 1-D simulations shows the same trend [triangles, Fig. 105.6(d)], but the absolute value, as remarked earlier, is significantly smaller.

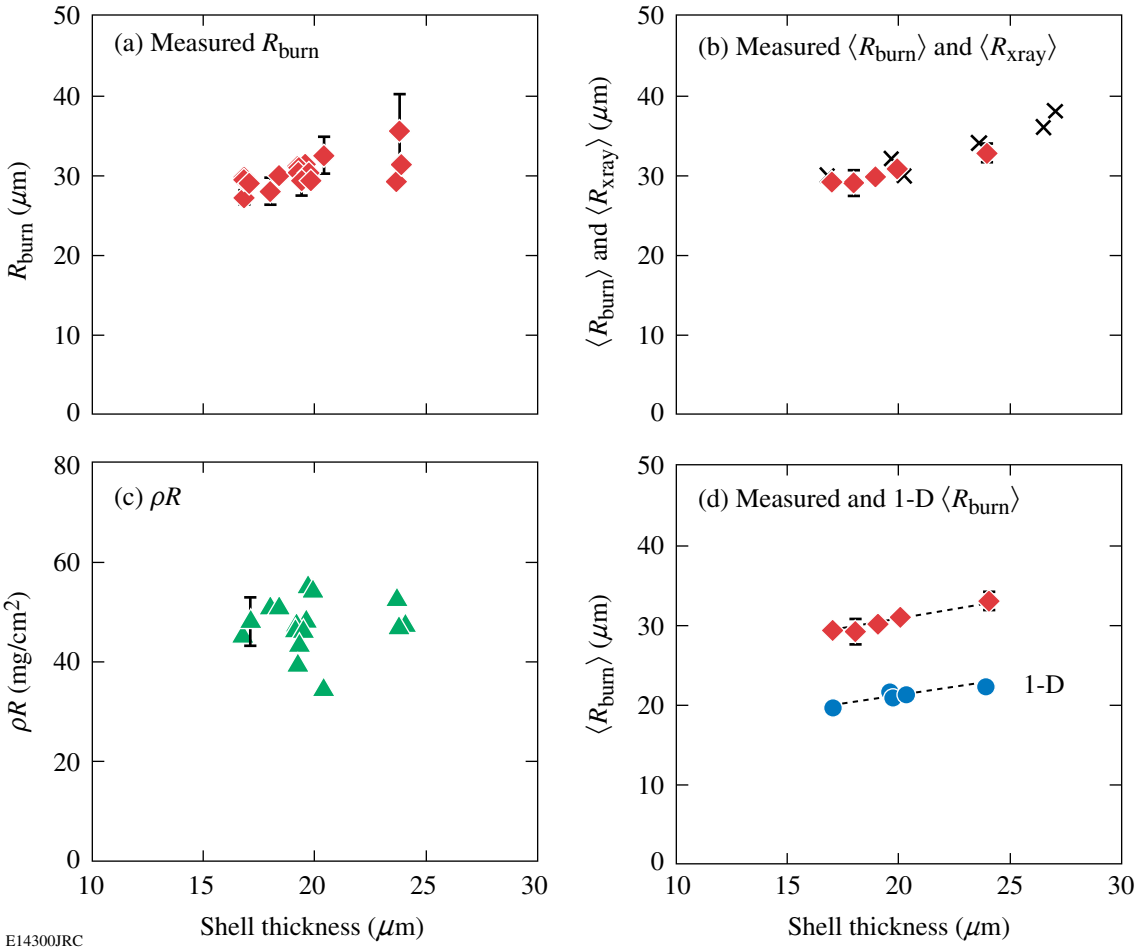

Figure 105.6
(a) The dependence of R_{burn} on plastic shell thickness provides information about mix and convergence.[2–10] (b) The trend is more obvious when the R_{burn} data for similar capsule thicknesses are averaged (diamonds). The fuel–shell interface estimates [R_{xray} (×'s)] for these implosions and others demonstrate virtually the same trend. (c) The areal densities ρR measured for the same implosions were only weakly dependent on shell thickness. (d) Predicted values of R_{burn} from 1-D simulations (circles) show the same trend as the measurements but lower values.

Summary and Discussion

In summary, we have described methods for measuring nuclear burn region sizes and presented the first measurements for a wide range of direct-drive implosion conditions, identifying systematic changes in burn region size due to changes in laser conditions and fuel capsule parameters. These measurements complement our related studies demonstrating systematic relationships between drive asymmetry, shell asymmetry, and burn asymmetry.[11,13] Collectively, this work demonstrates the practicality and usefulness of emission imaging of nuclear burn, which directly reveals the spatial distributions of the fusion reactions that are the end result of all physical processes affecting capsule implosions.

Starting with laser drive conditions, it was shown that the burn radius in capsules with thin (~2-μm) glass shells and 18-atm fills varies strongly with total laser energy, going from ~35 μm at 6 kJ to 80 μm at 23 kJ (all with 1-ns square pulses). Most measurements to date for capsules with plastic shells have been at 23 kJ, so no conclusions were drawn here about energy variations (but future experiments may investigate this). Measurements also indicated that changing from the SG3 DPP's to the SG4 DPP's for 20-μm CH shells and 18-atm fills didn't significantly change shell convergence but did result in a somewhat smaller R_{burn} that may simply reflect the smaller initial shell radius; this is consistent with other measurements,[44] indicating that changing from SG3 DPP's to SG4 DPP's brought no significant improvement in overall implosion performance for such capsules. Data for comparing R_{burn} for SG3 DPP's and SG4 DPP's with 3.6-atm fill pressures are currently unavailable.

Looking next at capsule structure, it was seen that increasing the CH shell thickness from 17 to 24 μm for 18-atm fills resulted in the burn radius increasing from 30 μm to 33 μm, a modest change largely attributed to the slightly smaller convergence of the more massive, thicker shell capsules. Measurements have not yet been made for glass capsules with different shell thicknesses, but capsules with 2-μm glass shells have burn radii 2.5 times larger than capsules with 20-μm CH shells with equal laser energy (23 kJ) and fill pressures (18 atm). It was also demonstrated that reducing the D^3He fill pressure from 18 to 3.6 atm in 20-μm CH shells resulted in little change in shell convergence but a significant change in burn radius (from 31 μm to 25 μm), a reduction largely attributed to increased fuel–shell mix for the more unstable 3.6-atm implosions. These data and interpretations are consistent with previous measurements of fuel ρR versus gas pressure in implosions of DT-filled capsules,[4] and we anticipate that more experiments and comparisons with simulations will be devoted to studying and quantifying the effects of mix.

The burn data were compared with x-ray images, which have a long history with ICF and therefore provide a very important point of comparison. As discussed in the text, x-ray images and burn images reflect different aspects of the compressed capsules and there is considerable ambiguity about how they should be compared and interpreted; the x-rays are most sensitive to CH from the inner part of the shell that is in contact with, or mixed into, the hot fuel. What was found is that the characteristic radius R_{xray}, calculated as described in Ref. 14 and thought to be an indication of the inner boundary of hot CH, is usually comparable to the characteristic burn radius R_{burn}, which represents the median burn radius. There is, therefore, usually a radial overlap between the apparent burn region and the apparent inner CH location. This overlap may represent a region of atomic mix or a region where fingers of shell material extend into the fuel region, although interpretation of the x-ray images in the presence of mix is beyond the scope of this article. A crucial fact about all of the data displayed here is that wherever R_{xray} and R_{burn} measurements are available for comparison [Figs. 105.4(b), 105.5(b), and 105.6(b)], they are comparable to each other and changes in one are tracked almost precisely by changes in the other. This is a strong independent confirmation that changes in burn region size measurements reflect true changes in the compressed capsule structure.

The burn data and x-ray data were both compared with predictions of 1-D simulations. It was found that while the 1-D burn radii were similar to the measured radii for capsules with thin glass shells [Fig. 105.3(c)], the predicted burn radii for capsules with 20-μm CH shells are smaller than the measured values by about 30% for an 18-atm fill and 50% for a 3.6-atm fill (and the measured R_{xray} was also larger than predicted for the 18-atm fill). These discrepancies are qualitatively consistent with the discrepancies between predicted and measured values of areal density, which show that shell convergence is lower than predicted for all CH-shell capsules studied. The dependence on fill pressure suggests that mix or instabilities could be a contributing factor. For a given amount of radial shell convergence, mix would be expected to make the burn region smaller by cooling the outer fuel regions, but we saw in **Capsule Fill Pressure** (p. 6) that the convergence is very much smaller than predicted for lower fill pressures, probably because of mix. In addition, mix is known to truncate the burn in time, leading to a higher-than-predicted average radius during the burn interval. Another possible explanation for the simulation/measurement difference is preheat, which

results in reduced compression due to increased pressure. For the glass-shell implosions, on the other hand, the roles of mix, hydrodynamic instabilities, and preheat are expected to be substantially smaller at burn time in glass-shell implosions than in CH-shell implosions,[40] and this could account for the closer agreement between simulation and data found in all such cases. In the future we hope to see if 2-D and 3-D simulations come closer to predicting the measured average shell convergence and measured burn region size. A thorough search for systematic errors that could lead to artificially broadened burn image data has been made, but no sources of error that could be large enough to account for the discrepancy in burn radii for CH shells have yet been identified.[12,41]

Comparisons of our D^3He burn profiles with DT and DD burn profiles now being obtained by Disdier *et al.* on OMEGA with important new neutron imaging techniques[46] for hydrodynamically similar DT- and D_2-filled capsules are now being pursued and will be reported in the future. These comparisons could provide a test of consistency of the different burn imaging methods and could potentially provide information about ion temperature profiles (through the local ratios of reaction rates).

ACKNOWLEDGMENT

The authors express their gratitude to the OMEGA engineers and operations crew who supported these experiments. In addition, we would like to personally thank Michael Canavan, Candice Culligan, and Jocelyn Schaeffer for their continuous help. This work has been supported in part by LLE (Subcontract No. 412160-001G) and LLNL (Subcontract No. B543881), and by the U.S. Department of Energy Office of Inertial Confinement Fusion (Grant No. DE-FG03-03NA00058) and under Cooperative Agreement No. DE-FC52-92SF19460, the University of Rochester, and New York State Energy Research and Development Authority.

Appendix: Notes on Determining Radial Burn Profiles from Penumbral Images

As described in Ref. 11, it is possible to determine the radial profile $S(r)$ of nuclear reactions in a burn region assumed spherically symmetric by analyzing a penumbral image made using reaction products. The details of the approach used in this article are slightly different from what is described in Ref. 11, and we discuss them here, along with alternative approaches and sample analyses. We start with the idealized assumption that the imaging aperture has a perfectly defined hard edge; a penumbral image of a point source would be uniform within a circular area and zero outside. This assumption is not warranted for the imaging of DT burn with DT neutrons, but it was shown in Ref. 12 that it should be sufficiently accurate for imaging D^3He burn with D^3He protons. A few protons will scatter off the edge of the aperture, but their scattering angle is sufficiently large that they contribute only a small, relatively flat penumbral image background that disappears when the radial derivative is taken for analysis. In **Generalization to Apertures Without "Hard Edges" and Neutron Imaging** (p. 14), we discuss how this limitation can be removed either for neutron images or for small corrections with proton images if the effects of the aperture edge can be characterized.

1. The Problem

The surface brightness of the spherically symmetric burn region is

$$B(r) = \int_{-\infty}^{\infty} S\left(\sqrt{r^2 + \ell^2}\right) d\ell. \tag{10}$$

A penumbral image made with a hard-edged, round aperture of radius R_a is azimuthally symmetric with a radial profile $N(R)$ of detected protons per unit area, where R is the radius measured with respect to the center of the image. The radial derivative of this image can be written

$$\left.\frac{dN}{dR}\right|_{R = R_d + Mx} = -\frac{1}{4\pi M\left(L_1 + L_2\right)^2} P_c(x), \tag{11}$$

where

$$P_c(x) = R_d \int_{-\pi}^{\pi} B\left[\sqrt{x^2 + 2R_c\left(R_c + x\right)\left(1 - \cos\theta\right)}\right] \cos\theta \, d\theta. \tag{12}$$

In Eq. (11), L_1 and L_2 are the source–aperture and aperture–detector distances, $M = L_2/L_1$ is the geometric magnification of the penumbral camera, and $R_d \equiv (M + 1)R_a$ is the radius of the aperture image at the detector. In Eq. (12), $R_c = R_a(M + 1)/M$ is the radius of the aperture's projection at the location of the burn region, as seen from the detector, and the angle θ is measured relative to the center of this projection. As discussed in Ref. 11, $P_c(x)$ is a set of integrals through the surface brightness of the burn region along parallel paths that are curved but become straight in the limit $R_{\text{burn}}/R_c << 1$;

$$P_c(x) \xrightarrow{R_{\text{burn}}/R_a \to 0} P(x) = \int_{-\infty}^{\infty} B\left(\sqrt{x^2 + \ell^2}\right) d\ell. \tag{13}$$

$P_c(x)$ can be thought of as a 1-D projection of the surface brightness $B(r)$.

$P_c(x)$ can be obtained experimentally from dN/dR through Eq. (11) and, if $R_{\text{burn}}/R_c << 1$, it can be used to obtain $B(r)$

through Abel inversion. Similarly, $B(r)$ can be Abel inverted to obtain the source profile $S(r)$. If R_{burn}/R_c is not negligible, then the straight-line integral $P(x)$ can be calculated approximately from $P_c(x)$ before the Abel inversion process;[47]

$$P(x) \cong \sqrt{1 + x/R_c}\, P_c(x) = -4\pi M\left(L_1 + L_2\right)^2 \sqrt{\frac{R}{R_d}}\,\frac{dN}{dR}\bigg|_{R = R_d + Mx}. \tag{14}$$

A simple analytic solution for direct calculation of the double Abel inversion relating $S(r)$ to $P(x)$ was described in Ref. 48 in connection with a different application (imaging of a spherically symmetric source with a linear slit aperture);

$$S(r) = -\frac{1}{2\pi r}\frac{dP(x)}{dx}\bigg|_{x = r}. \tag{15}$$

Equation (15) works well for perfect data (no noise or other distortions, infinitesimal sampling width, and $R_{\text{burn}}/R_c << 1$), but it isn't ideal for the data discussed in this article, even though the data generally satisfy the condition $R_{\text{burn}}/R_c << 1$ for several reasons. First, the statistics aren't good enough even after the data are binned [see the caption of Fig. 105.1(a)] except for the high-yield glass-shell capsules. Second, it becomes inaccurate when the data are binned, since this is equivalent to imposing a finite sampling width and results in artificial broadening of the inferred $S(r)$ and smoothing of any feature that is not much larger than the sampling width.[49] Finally, it has a problem at $r = 0$ where, even if $P(0) \equiv 0$, any noise or measurement uncertainty in the data near $r = 0$ translates into uncertainties in S that become infinite as $r \to 0$ [this is not a defect in Eq. (15), but a consequence of the fact that the central emissivity value applies to a small volume and has very little effect on line integrals through the surface brightness]. Nevertheless, the direct method works away from $r = 0$ if statistics allow and its application to the current data are illustrated in **Direct Calculation of $S(r)$** (p. 13).

2. Inferring $S(r)$ from Least-Squares Fits

As with many Abel inversion applications, the statistics issue can be improved by fitting the raw data with analytic functions that automatically smooth out some of the statistical fluctuations in $P(x)$ and simultaneously enforce reasonable behavior at the singular point $r = 0$. In Ref. 11, we proposed the use of powers of parabolas to represent $S(r)$ because these map analytically to other powers of parabolas for $P(x)$; the experimental $P(x)$ can be fit to powers of a parabola and $S(r)$ found analytically. This makes possible a range of profile shapes for $S(r)$ varying from hollow to peaked, with the limiting peaked shape being a Gaussian when the power goes to infinity, and works well because many of the data sets analyzed are statistically consistent with a Gaussian shape for $S(r)$. With many data sets there were indications that slightly better fits might be achieved with a profile more peaked than Gaussian, however, so here we take a different approach that has several advantages.

Instead of using a set of functions to fit to $P(x)$ and analytically deducing $S(r)$ using Eq. (15), we start by representing $S(r)$ by the family of super- and sub-Gaussians

$$S(r) = S_0 e^{-\left(r/r_0\right)^{2/p}}, \tag{16}$$

where r_0 is the "1/e" radius and p is the "peakedness" of the emission profile ($p = 0$ is flat, $p = 1$ is Gaussian, and $p > 1$ is more centrally peaked than Gaussian). From a given trial function $S(r)$, the functions $B(r)$, $P_c(x)$, and dN/dR can be calculated numerically using Eqs. (10), (12), and (11). For comparison with experimental data, the predicted dN/dR must then be convolved with a boxcar function to model the actual binning used in tabulating the measured data. To determine the most probable profile $S(r)$, the parameters R_d, S_0, p, and r_0 are varied and the values leading to a minimum χ^2 fit of predicted to measured dN/dR are determined along with their statistical uncertainties.[50] The deduced $S(r)$ can then be described by S_0 (or by the total yield), p, and r_0 though, as shown below, it turns out to be more useful to parameterize the radial size by the mean yield-weighted burn radius $\langle r\rangle_s = \int rS(r)r^2dr \Big/ \int S(r)r^2dr$ or by the median burn radius $r_{S,\text{median}}$ containing half the yield rather than by r_0.

Figure 105.7 illustrates sample shapes of $S(r)$ with corresponding functions $B(r)$ and $P(x)$. We see immediately that small differences in the shape of $P(x)$ translate into much larger differences in the shape of $S(r)$, which is characteristic of inversion procedures. This means that finite errors in the raw data are amplified into much larger errors in the shape of $S(r)$, particularly for small r, though it will turn out that errors in the characteristic radius are not amplified by the inversion process.

Figure 105.8 illustrates what happens when this technique is applied to the measured dN/dR data shown in Figs. 105.1(a) and 105.1(e). Figures 105.8(a) and 105.8(d) show contour plots of total χ^2 versus p and r_0 (using the values of R_c and S_0 that minimize χ^2 at every point). In each case there is a well-defined location

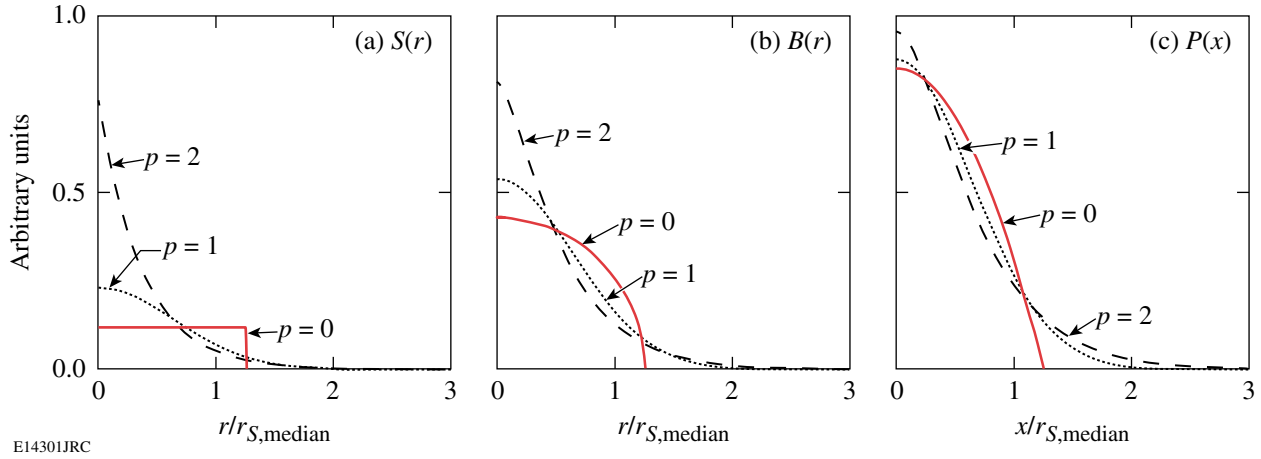

Figure 105.7
(a) $S(r)$ from Eq. (11) for $p = 0$, 1, and 2, normalized so that each curve has the same total yield. As discussed in the text, $r_{S,\text{median}}$ is the median radius (containing half the yield). (b) The corresponding curve for $B(r)$. (c) $P(x)$ for the case of no data binning. Note that hollow profiles of $S(r)$ can easily be added to this family of functions.

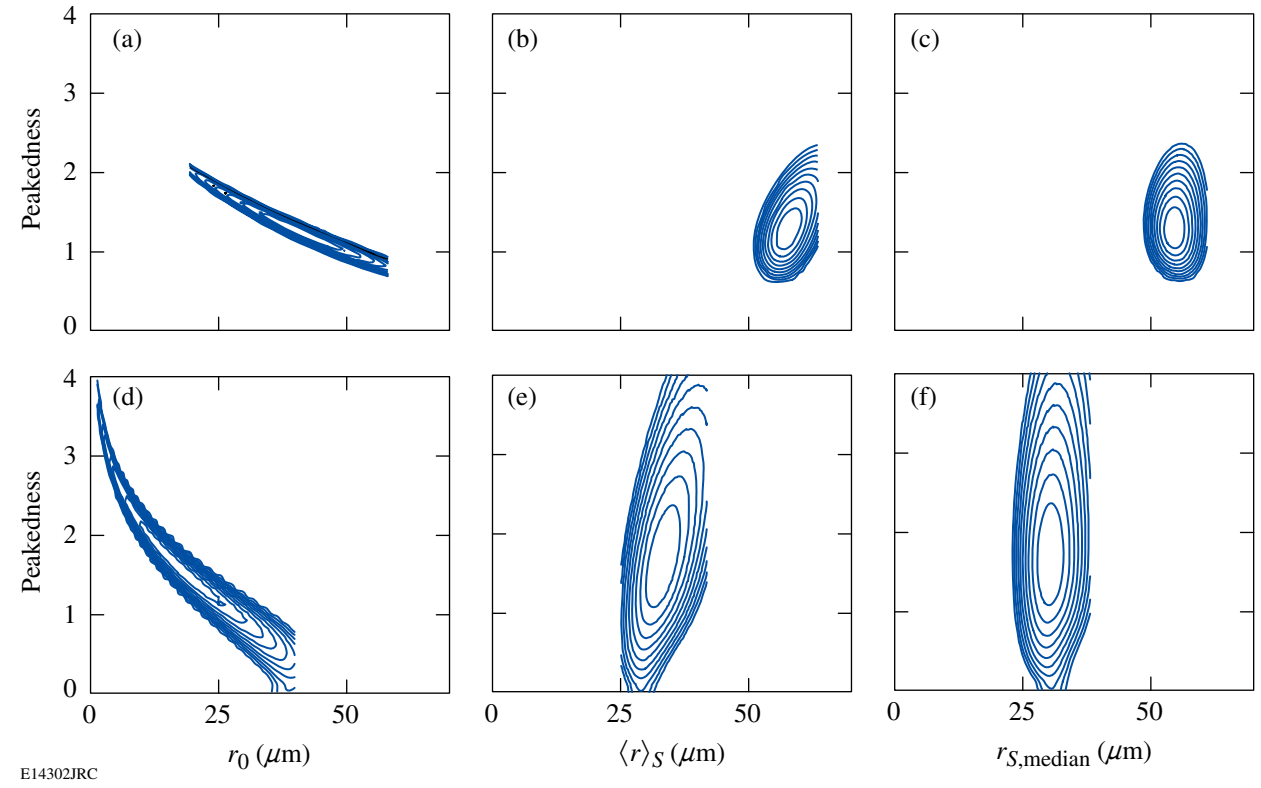

Figure 105.8
Contours of total χ^2 for fits to two real data sets as a function of the shape parameter p and either the $1/e$ radius r_0, $\langle r \rangle_S$, or $r_{S,\text{median}}$. The upper three plots correspond to shot 27456, while the lower plots correspond to shot 35176. In each case, the contour levels correspond to $\chi^2_{\text{minimum}} + 1, \chi^2_{\text{minimum}} + 2, \ldots$.

corresponding to the best fit (lowest χ^2). Figures 105.8(b) and 105.8(e) show the same contours parameterized by $\langle r\rangle_S$ rather than r_0, and Figs. 105.8(c) and 105.8(f) show parameterization by $r_{S,\text{median}}$. Notice that either $\langle r\rangle_S$ or $r_{S,\text{median}}$ is much more independent of the peakedness parameter p than r_0; the same conclusion has been reached using a wide range of functional forms for $S(r)$ and a wide range of data sets. The problem with r_0 is that a change in the central value of $S(r)$ changes the $1/e$ radius but has little effect on $P(x)$. In general, $r_{S,\text{median}}$ seems slightly better than $\langle r\rangle_S$, so henceforth we will define the characteristic burn radius R_{burn} to be $r_{S,\text{median}}$. Notice also that the percent statistical uncertainty in p is much larger than the uncertainty in R_{burn}. This is because errors in radial size do not get amplified in the inversion process, as can be shown analytically using Eq. (15) for the case $R_{\text{burn}}/R_a << 1$. The mean burn radius $\langle r\rangle_S$ is always exactly twice the average radius of $P(x)$; $\langle r\rangle_P \equiv \int xP(x)dx \Big/ \int P(x)dx = 0.5\langle r\rangle_S$, regardless of the shape of $S(r)$. This means that a fractional error in $\langle r\rangle_P$ results in the same fractional error in $\langle r\rangle_S$. A similar result holds for the median radius ($r_{P,\text{median}} = 0.44\ r_{S,\text{median}}$).

Figures 105.1(c), 105.1(g), 105.1(d), and 105.1(h) show the radial profiles of $S(r)$ and $B(r)$ corresponding to the same data and fits with uncertainties deduced from the fitting procedure. The largest uncertainties in $S(r)$ and $B(r)$ are at the center, and the uncertainties get larger with each level of inversion. The large uncertainties at $r = 0$ simply reflect the fact that the central emissivity has very little effect on penumbral images.

The family of functions represented by Eq. (16) doesn't extend to hollow profiles, but can easily be extended in that direction through the use of different functions. In addition, more complicated radial profiles using series expansions (e.g., of Chebyshev polynomials) can be used if statistics allow. But if yields are high enough, the direct calculation of $S(r)$ becomes practical.

3. Direct Calculation of $S(r)$

Subject to the conditions discussed in **The Problem** (p. 10), Eq. (15) allows direct calculation of $S(r)$ from $P(x)$ calculated with Eq. (14). Figure 105.9 shows how this works out for the two implosions analyzed above. This approach requires knowledge of R_d; for the calculations illustrated in Fig. 105.9, the values of R_d inferred from the fitting method were used. In each case the binning width was made as small as possible, consistent with the counting statistics. Shot 27456 has a high enough proton yield (~2×10^{10}) to make this method work for $r \gtrsim R_{\text{burn}}/3$; as r is reduced, the calculated values start to fall because of the effects of binning near the central peak, and as r approaches 0 the result is completely unreliable because of the singularity in Eq. (15). The yield is much lower for shot 37156 (~4×10^8), so the statistical errors on the calculated values of $S(r)$

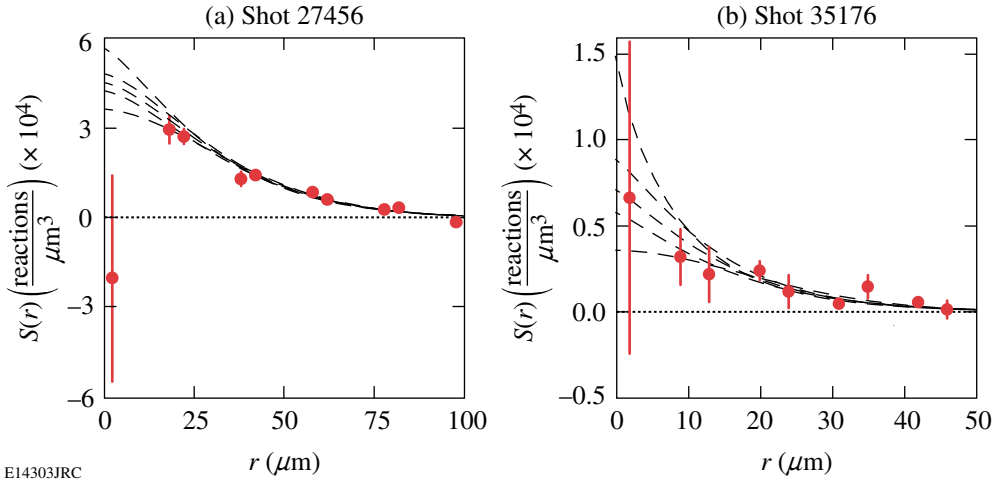

Figure 105.9
Results of applying the direct inversion method to data from shots (a) 27456 and (b) 35176. The plotted data points with error bars result from the application of Eq. (14) to the dN/dR data shown in Figs. 105.1(a) and 105.1(e); the data were binned slightly differently [with radial bins at the detector equivalent to bins in the burn region of 20 μm for (a) and 11 μm for (b), the effective ratios of bin width to R_{burn} were 0.37 and 0.41, respectively]. The uneven spacing of the data points reflects the fact that values of $S(r)$ were calculated from $P(x)$ for both positive and negative x, and S values at negative r values were reflected to positive r. The thin dashed lines correspond to the profiles shown in Figs. 105.1(d) and 105.1(h), including the error envelope.

are much larger and the shape of $S(r)$ is somewhat ill defined. The calculated value near $r = 0$ happened to be about right, but this was partly a matter of luck; changing the binning resulted in erratic values.

4. Generalization to Apertures Without "Hard Edges" and Neutron Imaging

If a penumbral-imaging aperture has a perfect, opaque edge, then the radial derivative dN/dR of a penumbral image of a point source will be a delta function. If not, and if dN/dR for a point source can be either calculated or measured, then it can be incorporated directly into the method described in **Inferring $S(r)$ from Least-Squares Fits** (p. 11). Before comparison with measured values of dN/dR, each predicted function calculated from a trial function $S(r)$ through Eqs. (10), (12), and (11) need only be convolved by an appropriate smearing function F before being convolved by the boxcar function that models the data binning. $F(R')$ is simply dN/dR for a point source evaluated at $R = R_d + R'$ and normalized to have unit integral. If the direct-calculation method is to be used instead of the least-squares fitting method, then the data must be deconvolved to remove the effect of F.

REFERENCES

1. J. Nuckolls *et al.*, Nature **239**, 139 (1972).
2. J. D. Lindl, *Inertial Confinement Fusion: The Quest for Ignition and Energy Gain Using Indirect Drive* (Springer-Verlag, New York, 1998).
3. S. Atzeni and J. Meyer-ter-Vehn, *The Physics of Inertial Fusion: Beam Plasma Interaction, Hydrodynamics, Hot Dense Matter*, International Series of Monographs on Physics (Clarendon Press, Oxford, 2004).
4. C. K. Li, F. H. Séguin, J. A. Frenje, S. Kurebayashi, R. D. Petrasso, D. D. Meyerhofer, J. M. Soures, J. A. Delettrez, V. Yu. Glebov, P. B. Radha, F. J. Marshall, S. P. Regan, S. Roberts, T. C. Sangster, and C. Stoeckl, Phys. Rev. Lett. **89**, 165002 (2002).
5. D. D. Meyerhofer, J. A. Delettrez, R. Epstein, V. Yu. Glebov, V. N. Goncharov, R. L. Keck, R. L. McCrory, P. W. McKenty, F. J. Marshall, P. B. Radha, S. P. Regan, S. Roberts, W. Seka, S. Skupsky, V. A. Smalyuk, C. Sorce, C. Stoeckl, J. M. Soures, R. P. J. Town, B. Yaakobi, J. D. Zuegel, J. Frenje, C. K. Li, R. D. Petrasso, D. G. Hicks, F. H. Séguin, K. Fletcher, S. Padalino, M. R. Freeman, N. Izumi, R. Lerche, T. W. Phillips, and T. C. Sangster, Phys. Plasmas **8**, 2251 (2001).
6. P. B. Radha, J. Delettrez, R. Epstein, V. Yu. Glebov, R. Keck, R. L. McCrory, P. McKenty, D. D. Meyerhofer, F. Marshall, S. P. Regan, S. Roberts, T. C. Sangster, W. Seka, S. Skupsky, V. Smalyuk, C. Sorce, C. Stoeckl, J. Soures, R. P. J. Town, B. Yaakobi, J. Frenje, C. K. Li, R. Petrasso, F. Séguin, K. Fletcher, S. Padalino, C. Freeman, N. Izumi, R. Lerche, and T. W. Phillips, Phys. Plasmas **9**, 2208 (2002).
7. S. P. Regan, J. A. Delettrez, F. J. Marshall, J. M. Soures, V. A. Smalyuk, B. Yaakobi, V. Yu. Glebov, P. A. Jaanimagi, D. D. Meyerhofer, P. B. Radha, W. Seka, S. Skupsky, C. Stoeckl, R. P. J. Town, D. A. Haynes, Jr., I. E. Golovkin, C. F. Hooper, Jr., J. A. Frenje, C. K. Li, R. D. Petrasso, and F. H. Séguin, Phys. Rev. Lett. **89**, 085003 (2002).
8. C. R. Christensen, D. C. Wilson, C. W. Barnes, G. P. Grim, G. L. Morgan, M. D. Wilke, F. J. Marshall, V. Yu. Glebov, and C. Stoeckl, Phys. Plasmas **11**, 2771 (2004).
9. D. C. Wilson, C. W. Cranfill, C. Christensen, R. A. Forster, R. R. Peterson, H. M. Hoffman, G. D. Pollak, C. K. Li, F. H. Séguin, J. A. Frenje, R. D. Petrasso, P. W. McKenty, F. J. Marshall, V. Yu. Glebov, C. Stoeckl, G. J. Schmid, N. Izumi, and P. Amendt, Phys. Plasmas **11**, 2723 (2004).
10. P. B. Radha, V. N. Goncharov, T. J. B. Collins, J. A. Delettrez, Y. Elbaz, V. Yu. Glebov, R. L. Keck, D. E. Keller, J. P. Knauer, J. A. Marozas, F. J. Marshall, P. W. McKenty, D. D. Meyerhofer, S. P. Regan, T. C. Sangster, D. Shvarts, S. Skupsky, Y. Srebro, R. P. J. Town, and C. Stoeckl, Phys. Plasmas **12**, 032702 (2005).
11. F. H. Séguin, J. L. DeCiantis, J. A. Frenje, S. Kurebayashi, C. K. Li, J. R. Rygg, C. Chen, V. Berube, B. E. Schwartz, R. D. Petrasso, V. A. Smalyuk, F. J. Marshall, J. P. Knauer, J. A. Delettrez, P. W. McKenty, D. D. Meyerhofer, S. Roberts, T. C. Sangster, K. Mikaelian, and H. S. Park, Rev. Sci. Instrum. **75**, 3520 (2004).
12. J. L. DeCiantis, F. H. Séguin, J. A. Frenje, V. Berube, M. J. Canavan, C. D. Chen, S. Kurebayashi, C. K. Li, J. R. Rygg, B. E. Schwartz, R. D. Petrasso, J. A. Delettrez, S. P. Regan, V. A. Smalyuk, J. P. Knauer, F. J. Marshall, D. D. Meyerhofer, S. Roberts, T. C. Sangster, C. Stoeckl, K. Mikaelian, H. S. Park, and H. F. Robey, "Proton Core Imaging of the Nuclear Burn in Inertial Confinement Fusion Implosions," to be published in Review of Scientific Instruments (see also LLE Review Quarterly Report **104**, p. 197).
13. F. H. Séguin, J. L. DeCiantis, J. A. Frenje, C. K. Li, J. R. Rygg, C. D. Chen, R. D. Petrasso, V. A. Smalyuk, F. J. Marshall, J. A. Delettrez, J. P. Knauer, P. W. McKenty, D. D. Meyerhofer, S. Roberts, T. C. Sangster, H. S. Mikaelian, and H. S. Park, Bull. Am. Phys. Soc. **49**, 63 (2004); *ibid.* "Measured Effects of Drive Asymmetry and Shell Asymmetry on Nuclear Burn Region Symmetry in Direct-Drive ICF implosions," to be submitted to Physics of Plasmas.
14. S. P. Regan, J. A. Delettrez, R. Epstein, P. A. Jaanimagi, B. Yaakobi, V. A. Smalyuk, F. J. Marshall, D. D. Meyerhofer, W. Seka, D. A. Haynes, Jr., I. E. Golovkin, and C. F. Hooper, Jr., Phys. Plasmas **9**, 1357 (2002).
15. D. Ress *et al.*, Rev. Sci. Instrum. **66**, 579 (1995).
16. V. A. Smalyuk, T. R. Boehly, L. S. Iwan, T. J. Kessler, J. P. Knauer, F. J. Marshall, D. D. Meyerhofer, C. Stoeckl, B. Yaakobi, and D. K. Bradley, Rev. Sci. Instrum. **72**, 635 (2001).
17. F. J. Marshall, J. A. Delettrez, R. Epstein, V. Yu. Glebov, D. R. Harding, P. W. McKenty, D. D. Meyerhofer, P. B. Radha, W. Seka, S. Skupsky,

V. A. Smalyuk, J. M. Soures, C. Stoeckl, R. P. Town, B. Yaakobi, C. K. Li, F. H. Séguin, D. G. Hicks, and R. D. Petrasso, Phys. Plasmas **7**, 2108 (2000).

18. F. H. Séguin, C. K. Li, J. A. Frenje, S. Kurebayashi, R. D. Petrasso, F. J. Marshall, D. D. Meyerhofer, J. M. Soures, T. C. Sangster, C. Stoeckl, J. A. Delettrez, P. B. Radha, V. A. Smalyuk, and S. Roberts, Phys. Plasmas **9**, 3558 (2002).

19. F. H. Séguin, J. A. Frenje, C. K. Li, D. G. Hicks, S. Kurebayashi, J. R. Rygg, B.-E. Schwartz, R. D. Petrasso, S. Roberts, J. M. Soures, D. D. Meyerhofer, T. C. Sangster, J. P. Knauer, C. Sorce, V. Yu. Glebov, C. Stoeckl, T. W. Phillips, R. J. Leeper, K. Fletcher, and S. Padalino, Rev. Sci. Instrum. **74**, 975 (2003).

20. F. H. Séguin, C. K. Li, D. G. Hicks, J. A. Frenje, K. M. Green, R. D. Petrasso, J. M. Soures, D. D. Meyerhofer, V. Yu. Glebov, C. Stoeckl, P. B. Radha, S. Roberts, C. Sorce, T. C. Sangster, M. D. Cable, S. Padalino, and K. Fletcher, Phys. Plasmas **9**, 2725 (2002).

21. C. K. Li, F. H. Séguin, J. A. Frenje, R. D. Petrasso, R. Rygg, S. Kurebayashi, B. Schwartz, R. L. Keck, J. A. Delettrez, J. M. Soures, P. W. McKenty, V. N. Goncharov, J. P. Knauer, F. J. Marshall, D. D. Meyerhofer, P. B. Radha, S. P. Regan, T. C. Sangster, W. Seka, and C. Stoeckl, Phys. Plasmas **10**, 1919 (2003).

22. R. D. Petrasso, J. A. Frenje, C. K. Li, F. H. Séguin, J. R. Rygg, B. E. Schwartz, S. Kurebayashi, P. B. Radha, C. Stoeckl, J. M. Soures, J. Delettrez, V. Yu. Glebov, D. D. Meyerhofer, and T. C. Sangster, Phys. Rev. Lett. **90**, 095002 (2003).

23. C. K. Li, D. G. Hicks, F. H. Séguin, J. A. Frenje, R. D. Petrasso, J. M. Soures, P. B. Radha, V. Yu. Glebov, C. Stoeckl, D. R. Harding, J. P. Knauer, R. L. Kremens, F. J. Marshall, D. D. Meyerhofer, S. Skupsky, S. Roberts, C. Sorce, T. C. Sangster, T. W. Phillips, M. D. Cable, and R. J. Leeper, Phys. Plasmas **7**, 2578 (2000).

24. M. C. Richardson, P. W. McKenty, F. J. Marshall, C. P. Verdon, J. M. Soures, R. L. McCrory, O. Barnouin, R. S. Craxton, J. Delettrez, R. L. Hutchison, P. A. Jaanimagi, R. Keck, T. Kessler, H. Kim, S. A. Letzring, D. M. Roback, W. Seka, S. Skupsky, B. Yaakobi, S. M. Lane, and S. Prussin, in *Laser Interaction and Related Plasma Phenomena*, edited by H. Hora and G. H. Miley (Plenum Publishing, New York, 1986), Vol. 7, pp. 421–448.

25. J. Delettrez, R. Epstein, M. C. Richardson, P. A. Jaanimagi, and B. L. Henke, Phys. Rev. A **36**, 3926 (1987).

26. K. A. Nugent and B. Luther-Davies, J. Appl. Phys. **58**, 2508 (1985).

27. D. Ress *et al.*, Rev. Sci. Instrum. **59**, 1694 (1988).

28. R. A. Lerche *et al.*, Laser Part. Beams **9**, 99 (1991).

29. L. Disdier, R. A. Lerche, J. L. Bourgade, and V. Yu. Glebov, Rev. Sci. Instrum. **75**, 2134 (2004).

30. Y.-W. Chen *et al.*, Opt. Commun. **73**, 337 (1989).

31. M. Nakai *et al.*, Rev. Sci. Instrum. **61**, 3235 (1990).

32. A. P. Fews *et al.*, Phys. Rev. Lett. **73**, 1801 (1994).

33. T. R. Boehly, D. L. Brown, R. S. Craxton, R. L. Keck, J. P. Knauer, J. H. Kelly, T. J. Kessler, S. A. Kumpan, S. J. Loucks, S. A. Letzring, F. J. Marshall, R. L. McCrory, S. F. B. Morse, W. Seka, J. M. Soures, and C. P. Verdon, Opt. Commun. **133**, 495 (1997).

34. Y. Lin, T. J. Kessler, and G. N. Lawrence, Opt. Lett. **20**, 764 (1995).

35. S. Skupsky, R. W. Short, T. Kessler, R. S. Craxton, S. Letzring, and J. M. Soures, J. Appl. Phys. **66**, 3456 (1989).

36. S. P. Regan, J. A. Marozas, R. S. Craxton, J. H. Kelly, W. R. Donaldson, P. A. Jaanimagi, D. Jacobs-Perkins, R. L. Keck, T. J. Kessler, D. D. Meyerhofer, T. C. Sangster, W. Seka, V. A. Smalyuk, S. Skupsky, and J. D. Zuegel, J. Opt. Soc. Am. B **22**, 998 (2005).

37. T. R. Boehly, V. A. Smalyuk, D. D. Meyerhofer, J. P. Knauer, D. K. Bradley, R. S. Craxton, M. J. Guardalben, S. Skupsky, and T. J. Kessler, J. Appl. Phys. **85**, 3444 (1999).

38. R. A. Forties and F. J. Marshall, Rev. Sci. Instrum. **76**, 073505 (2005).

39. C. K. Li, F. H. Séguin, D. G. Hicks, J. A. Frenje, K. M. Green, S. Kurebayashi, R. D. Petrasso, D. D. Meyerhofer, J. M. Soures, V. Yu. Glebov, R. L. Keck, P. B. Radha, S. Roberts, W. Seka, S. Skupsky, C. Stoeckl, and T. C. Sangster, Phys. Plasmas **8**, 4902 (2001).

40. M. D. Rosen and J. H. Nuckolls, Phys. Fluids **22**, 1393 (1979).

41. Calculations showed insignificant image broadening associated with proton scattering in the capsule, aperture, and detector filters, while experiments showed no indication of different results with different aperture size or magnification. Neither experiments nor simulations revealed any serious field effects.[12]

42. V. Yu. Glebov, C. Stoeckl, T. C. Sangster, S. Roberts, G. J. Schmid, R. A. Lerche, and M. J. Moran, Rev. Sci. Instrum. **75**, 3559 (2004).

43. The plotted R_{burn} and $\langle \rho R \rangle$ results for individual implosions already represent a mean value of the measurements obtained from that implosion; there were as many as six measurements of R_{burn}[12] and five of ρR for each implosion. When the mean value is calculated for an implosion type, all these measurements are weighted equally.

44. S. P. Regan, J. A. Delettrez, V. Yu. Glebov, V. N. Goncharov, J. A. Marozas, F. J. Marshall, P. W. McKenty, D. D. Meyerhofer, P. B. Radha, T. C. Sangster, V. A. Smalyuk, C. Stoeckl, J. A. Frenje, C. K. Li, R. D. Petrasso, and F. H. Séguin, Bull. Am. Phys. Soc **49**, 62 (2004).

45. The SG3 R_{xray} data point was taken from a hydrodynamically equivalent 15-atm, D_2 gas-fill implosion (shot 22546).[7] The substitution is reasonable; similar R_{xray} results are obtained from D_2 and D^3He gas implosions (J. L. DeCiantis, "Proton Emission Imaging of the Nuclear Burn in Inertial Confinement Fusion Experiments," M.S. thesis, Massachusetts Institute of Technology, 2005).

46. L. Disdier, A. Rouyer, I. Lantuejoul, O. Landuas, J. L. Bourgade, T. C. Sangster, V. Yu. Glebov, and R. A. Lerche, "Inertial Confinement Fusion Neutron Images," to be published in Physics of Plasmas.

47. The correction factor $\sqrt{1 + x/R_c} = \sqrt{R/R_d}$ in Eq. (14) can be found by calculating the integrals for a circular disk with uniform surface brightness and keeping the lowest-order terms. Since any radial profile of surface brightness can be made up from a superposition of disks, the result is independent of radial profile. This is a better correction than that shown in Eq. (7) of Ref. 11, which was found empirically. In any case, the correction is too small to be important for the data considered here.

48. C. M. Vest and D. G. Steel, Opt. Lett. **3**, 54 (1978).

49. M. M. Mueller, Opt. Lett. **4**, 351 (1979).

50. The parameter R_d is the radius on the detector corresponding to the center of the penumbra. In principle, this value is known in advance from the dimensions of the imaging system, but it must be known very accurately, and including it as a fit parameter allows for the possibility of small errors in camera positioning. Two more parameters that need to be known are the coordinates of the center of the penumbral image. This is found by doing a simplified version of the analysis described in the text, but varying the assumed center coordinates and finding the values that give the smallest burn radius (since any displacement from the true center broadens the average penumbra and the inferred burn radius).